



High efficient solar hydrogen generation by modulation of Co-Ni sulfide (220) surface structure and adjusting adsorption hydrogen energy



Haibo Gao ^{a,b}, Wenlong Zhen ^{a,b}, Jiantai Ma ^a, Gongxuan Lu ^{b,*}

^a State Key Laboratory of Applied Organic Chemistry, College of Chemistry and Chemical Engineering, Lanzhou University, Lanzhou, China

^b State Key Laboratory for Oxo Synthesis and Selective Oxidation, Lanzhou Institute of Chemical Physics, Chinese Academy of Sciences, Lanzhou, China

ARTICLE INFO

Article history:

Received 8 November 2016

Received in revised form 4 January 2017

Accepted 18 January 2017

Available online 21 January 2017

Keywords:

CoNi sulfide cocatalyst

Low hydrogen adsorption energy

The (220) facet adjusting

Low overpotential

High efficiency for visible photocatalytic hydrogen generation

ABSTRACT

Low overpotential co-catalyst is a key component for a photocatalyst in photocatalytic hydrogen generation. Dual transition metal sulfide is known as a candidate in replacing noble metal. Its property is highly dependent on its surface structure and chemical state. In this paper, we found that the hydrogen adsorption energy (ΔG_H) on various dual metal sulfide $\text{Co}_x\text{Ni}_{4-x}\text{S}_4$ co-catalysts could be adjusted by variation of Co and Ni ratio. The hydrogen adsorption energies over Co and Ni sites in $\text{Co}_2\text{Ni}_2\text{S}_4$ catalyst were 548.7 and 506 kJ mol^{-1} respectively, while the corresponding energies over CoNi_3S_4 and Co_3NiS_4 catalysts were much higher than the data over $\text{Co}_2\text{Ni}_2\text{S}_4$ catalyst. It was found that the XRD peaks of (220) facet of $\text{Co}_x\text{Ni}_{4-x}\text{S}_4$ shifted from 26.27° to 26.53° when Co/Ni ration varied from 3 to 1, while other facet XRD peak location did not changed, indicating surface structure of (220) facet was adjusted and could be artificially controlled. In optimized $\text{Co}_2\text{Ni}_2\text{S}_4$ co-catalyst surface, the intermediate during hydrogen formation is much more stable than over other $\text{Co}_x\text{Ni}_{4-x}\text{S}_4$ co-catalyst. The surface chemical state were also controlled by Co and Ni ratio, the corresponding $\text{Co } 2p_{3/2}$ of $\text{Co}_x\text{Ni}_{4-x}\text{S}_4@\text{MIL-101}$ samples shifted to higher energy side when the Co/Ni ratio changed from 3:1 to 1:3, while $\text{Ni } 2p_{3/2}$ shifted to low energy side, which implied the composition and surface structure change leading to subtle variation of surface chemical state, as a result, it affected the properties of co-catalyst. The electrochemical and fluorescence measurement results indicated that the $\text{Co}_2\text{Ni}_2\text{S}_4@\text{MIL-101}$ exhibited the highest transient photocurrent, the lowest overpotential (-0.33 V) and the longer fluorescence lifetime (1.49 ns). The obtained $\text{Co}_2\text{Ni}_2\text{S}_4@\text{MIL-101}$ catalyst exhibited excellent activity for hydrogen generation (882.7 $\mu\text{mol H}_2$ in 2 h), better stability and higher apparent quantum efficiency (AQE) of $\sim 48.9\%$ under visible light irradiation (>430 nm). The high photocatalytic efficiency of $\text{Co}_2\text{Ni}_2\text{S}_4@\text{MIL-101}$ catalyst can be attributed to the low ΔG_H over $\text{Co}_2\text{Ni}_2\text{S}_4$ co-catalyst, stable reaction intermediate during hydrogen formation and better photoelectrochemical properties.

© 2017 Elsevier B.V. All rights reserved.

1. Introduction

The rapid depletion of fossil fuels (oil, gas, and coal) and growing environmental pollution have presented an acute need to develop alternative energy sources [1]. Hydrogen energy is considered to be one of promising candidates for replacing petroleum fuels in the future due to its high energy density and the environment benign properties [2,3]. Many efforts have devoted to the production of hydrogen from renewable resources, including biomass catalytic steam reforming/gasification [4], alkanes reforming [5], enzymatic

approaches [6] and photocatalysis [7]. Among them, using free and sustainable solar energy to produce hydrogen is a promising route because there is no net carbon dioxide emission in this process, typically photocatalytic water splitting for hydrogen evolution reaction (HER). Up to now, noble metals based (such as Pt, Ru and Rh) co-catalysts are the most efficient photocatalysts due to its lower overpotential for HER and suitable Fermi level for accepting photogenerated electrons [8–11]. However, the high cost and limited reserves severely prohibit their large sale usage. Therefore, developing low cost and effective HER photocatalysts still remains objectives [12–14]. To improve the efficiency of hydrogen generation, one key obstacle is reducing the overpotential of the co-catalyst. To low the overpotential, it is necessary to develop co-catalyst with active exposed facet, [15] high dispersion active

* Corresponding author.

E-mail address: gxl@lzb.ac.cn (G. Lu).

species, [16] which can offer fast charge transfer and low surface adsorption energy for hydrogen formation.

Recently, metal sulfides have attracted considerable attention as photocatalysts for HER under visible light because of its noble metal like properties. [17–19] Li et al. reported that the MoS₂/RGO hybrid with highly exposed edges and low overpotential exhibited excellent HER activity [15]. Likewise, Kong et al. showed that highly-dispersed NiS_x anchored on graphene surface exhibited higher photocatalytic activity for HER than Pt co-catalyst [16]. Composite systems are considered promising because of synergistic effects, such as better visible light absorption and improved photostability [20]. The quantum efficiency of solar hydrogen evolution over Cd_{0.5}Zn_{0.5}S nanorods reached 62%; the twin-induced one-dimensional homojunctions exhibited higher activity for HER and better structure for charge separation than simple sulfide. The homojunctions permitted one to adjust the band structures of semiconductors to the specific state in a more precise way, which enhanced the catalyst performance. [21] For example, Kudo et al. reported the sulfide solid solution photocatalysts AgInS₂–CuInS₂–ZnS were highly active for H₂ evolution due to about 1.5 eV band gap [22].

The hydrogen generation process usually occurs *via* three steps, H⁺ adsorption, H⁺ reduction, H atom formation and hydrogen desorption in sequence. The adsorption of H atom on the cocatalyst surface was the key factor for the HER, which reflected the extent of the adsorption process and driving force [23–25]. The kinetics of the HER was controlled by the energy of adsorbed state hydrogen (H_{ads}) over the catalyst surface atoms [26]. Marković et al. reported the activity of platinum single-crystal surfaces for the HER in acid and alkaline solution increased in the sequence (111)<(100)<(110). Their activation energies were Pt (110)≈18 kJ/mol, Pt (100)≈12 kJ/mol and Pt (110)≈9.5 kJ/mol, respectively. This difference in activation energy with the crystal facet is due to the structure-sensitive heats of adsorption of the active intermediate [27]. Experiments and density functional theory (DFT) calculations revealed that there were synergistically promoted the proton adsorption and reduction during HER. [28,29] Therefore, the development of efficient HER catalyst that functionally changing the structure to reduce surface adsorption energy and overpotential is a high challenging in achieving high hydrogen generation activity. [30–32]

More recently, metal-organic frameworks (MOFs) had emerged as catalyst support mainly because of its high surface areas for loading high dispersion active components and regular channel for reactant diffusion [33–35]. Herein, we reported high efficient co-catalyst Co_xNi_{4-x}S₄ particles anchored in the frameworks of MIL-101 (Co_xNi_{4-x}S₄@MIL-101) for photocatalytic hydrogen evolution from water. By regulating the content of cobalt and nickel, the catalyst Co₂Ni₂S₄@MIL-101 exhibited low hydrogen adsorption energy (506 kJ mol⁻¹) and low overpotential (−0.33 V) for proton reduction, which led to higher activity for HER. That co-catalyst exhibited the larger transient photocurrent and longer fluorescence lifetime (1.49 ns). The highest apparent quantum efficiency (~48.9%) was accomplished under 430 nm illuminations. The Co₂Ni₂S₄@MIL-101 catalyst showed potential application in replacing precious metal for HER.

2. Experimental

2.1. Materials

All chemicals were analytical pure and used without further purification. Chromic nitrate nonahydrate (Cr(NO₃)₃·9H₂O, Tianjin Kermel Chemical Reagent Co., Ltd., AR, ≥99.0%), hydrofluoric acid (HF, Kishida Chemical Co., Ltd., ≥46.0%), terephthalic acid (H₂BDC,

Shanghai KEFENG Chemical Reagent Co., Ltd., ≥99.0%), Cobalt(II) acetate tetrahydrate (Co(CH₃COO)₂·4H₂O, J&K Scientific Ltd., AR, ≥99.0%), Nickel(II) acetate tetrahydrate (Ni(CH₃COO)₂·4H₂O, J&K Scientific Ltd., AR, ≥99.0%), dimethyl sulfoxide (DMSO, Tianjin NO.2 Reagent Co., Ltd., AR, ≥99.0%), acetone (Tianjin Kermel Chemical Reagent Co., Ltd., AR, ≥99.5%), ammonium fluoride (NH₄F, Tianjin Kermel Chemical Reagent Co., Ltd., AR, ≥96.0%), ethanol (C₂H₅OH, Tianjin NO.2 Reagent Co., Ltd., AR, ≥97.0%) and triethanolamine (TEOA, Xilong Chemical Co., Ltd., AR, ≥98.0%) were used as received. De-ionized water with a specific resistance of 18.2 MΩ cm was obtained by reverse osmosis followed by ion-exchange and filtration (Milli-QTM Advantage A10TM).

2.2. Synthesis of MIL-101

MIL-101 was synthesized according to the reported procedure. Terephthalic acid (1.66 g, 10.0 mmol), Cr(NO₃)₃·9H₂O (4.10 g, 10.0 mmol), aqueous HF (0.5 mL, 46 wt%) and de-ionized water (70 mL) were placed in a Teflon-liner autoclave (100 mL) and heated at 220 °C for 8 h. After natural cooling, the suspension was centrifuged to separate the green powder of MIL-101 with formula Cr₃F(H₂O)₂O[(O₂C)C₆H₄(CO₂)]₃·nH₂O (n≤25), and then further purified by solvothermal treatment in ethanol at 80 °C for 24 h [36,37]. The green solid product was soaked in NH₄F (1 M) solution at 70 °C for 24 h to eliminate the terephthalic acid inside the pores of MIL-101 and immediately filtered resulting green solid was finally dried overnight at 150 °C under vacuum for further use [38].

2.3. Syntheses of Co_xNi_{4-x}S₄@MIL-101

The 20%Co₂Ni₂S₄@MIL-101 nanoparticles were prepared by sequentially adding 3.2 mmol of Co(CH₃COO)₂·4H₂O and 3.2 mmol Ni(CH₃COO)₂·4H₂O of to a 50 mL DMSO solution by vigorous stirring to form a stable suspension. Then 1.1648 g MIL-101 was added the aforementioned solutions. After that, the reaction mixture was further stirred for 30 min, transferred into a Teflon-lined autoclave (80 mL), and heated to 180 °C for 12 h at a ramping speed of 30 °C min⁻¹. After natural cooling, the product was separated by centrifugation, washed several times with acetone and absolute ethanol, and then dried in a vacuum oven at 60 °C for 8 h. Preparation of other Co_xNi_{4-x}S₄@MIL-101 nanoparticles is the same as the synthesis of 20%Co₂Ni₂S₄@MIL-101 except employing different molar ratios and a total molar amount of 6.4 mmol of Co(CH₃COO)₂·4H₂O and Ni(CH₃COO)₂·4H₂O [39].

2.4. Activities measurement

The photocatalytic activity test was carried out at a constant temperature of 20 °C. Measurements of photocatalytic H₂ evolution activity were performed in a sealed Pyrex flask (175 mL) with a flat window (an efficient irradiation area of 10.2 cm²) and a silicone rubber septum for sampling. A 300-W Xenon lamp equipped with a 420 nm cutoff filter was used as a light source. The reactant mixture was prepared by dispersing 50 mg of powder photocatalyst and 69.1 mg Eosin Y (EY) in 100 mL of aqueous triethanolamine (TEOA, 10(v/v) %, pH 9) solution under ultrasonication and was purged with argon gas for 40 min before irradiation. During the photocatalytic process, 0.5 mL gas sample in the top of reactor was collected intermittently through the septum and the amount of hydrogen evolution was measured with gas chromatography (Agilent 6820, TCD, 13 × column, Ar carrier).

The apparent quantum efficiency (AQE) was measured under the same photocatalytic reaction conditions with irradiation light through a bandpass filter (430, 460, 490, 520, or 550 nm). Photon flux of the incident light was determined using a Ray virtual radiation actinometer (FU 100, silicon ray detector, light spectrum,

400–700 nm; sensitivity, $10\text{--}50 \mu\text{V} \mu\text{mol}^{-1} \text{m}^{-2} \text{s}^{-1}$). The sealed Pyrex flask wrapped with tin foil provide an effective and fixed light flat surface (an efficient irradiation area of 4.91 cm^2). The reaction solutions were irradiated for 30 min with bandpass filters for AQE tests on the H_2 production. The following equation was used to calculate the AQE.

$$\text{AQE} = \frac{2 \times \text{the number of evolved hydrogen molecules}}{\text{the number of incident photons}} \times 100\%$$

2.5. Photoelectro-chemical measurements

All the electrochemical measurements were measured on an electrochemical analyzer (CHI660A) in a homemade standard three-electrode cell. The working electrodes were prepared by drop-coating sample suspensions directly onto the pre-cleaned indium tin oxide glass (ITO glass) surface. Platinum foil was used as the counter electrode and a saturated calomel electrode (SCE) as the reference electrode. The supporting electrolyte was 10% (v/v) TEOA mixed 0.1 mol/L Na_2SO_4 aqueous solution. The surface area of the working electrode exposed to the electrolyte was about 0.95 cm^2 . The cathodic polarization curves were obtained using the linear sweep voltammetry (LSV) technique with a scan rate of 1 mV s^{-1} . For the preparation of working electrodes for photoelectrochemical measurements, $500 \mu\text{L}$ of EY aqueous solution ($1.0 \times 10^{-3} \text{ mol/L}$) was added onto the above catalyst film electrode surface and then dried. A 300-W Xe lamp equipped with an optical cutoff filter of 420 nm was used for excitation.

2.6. Characterization of the catalysts

The X-ray diffraction patterns (XRD) of the samples were recorded on a Rigaku B/Max-RB X-ray diffractometer with a nickel-filtered $\text{Cu K}\alpha$ radiation over a 2θ range of $2\text{--}85^\circ$ and a position sensitive detector using a step size of 0.017° and a step time of 15 s at 40 mA and 40 kV. X-ray photoelectron spectroscopy (XPS) analysis was performed using a VG Scientific ESCALAB 250Xi-XPS photoelectron spectrometer with an $\text{Al K}\alpha$ X-ray source. The binding energies were calibrated by the C1s binding energy of 284.7 eV. The specific surface areas of the catalysts were determined by N_2 adsorption-desorption measurements by employing the Brunauer-Emmet-Teller (BET) method (Micromeritics apparatus ASAP 2020 M) at 77 K. Transmission electron microscopy (TEM) and HRTEM images were taken with a Tecnai-G2-F30 field emission transmission electron microscope operating at accelerating voltage of 300 kV. UV-vis absorption spectra were obtained with a Hewlett-Packard 8453 spectrophotometer. Fourier transform infrared (FT-IR) spectra were performed on a Nicolet Nexus 870 with the wave number from 4000 to 400 cm^{-1} . The dispersion was measured by H_2 chemisorption using a Micromeritics Chemisorb 2750 Pulse Chemisorption System at 25°C .

3. Results and discussion

3.1. Calculation of hydrogen adsorption energy

Hydrogen evolution reaction in photocatalytic reaction is usually accompanied by electron transfer, which means that electrons transfer from the highest occupied molecular orbit (HOMO) of co-catalyst to the lowest unoccupied molecular orbit (LUMO) of H_2O , i.e., the HOMO electrons on co-catalyst transfer to H_2O , and then reduce H^+ to H atom consequently. The electrons transfer is easier from HOMO to LUMO when the ΔE is smaller. To simplify the calculations, cobalt and nickel were considered in the form of divalent state. The optimized geometry results of adsorbed H and related charge density of HOMO molecular orbital surface on

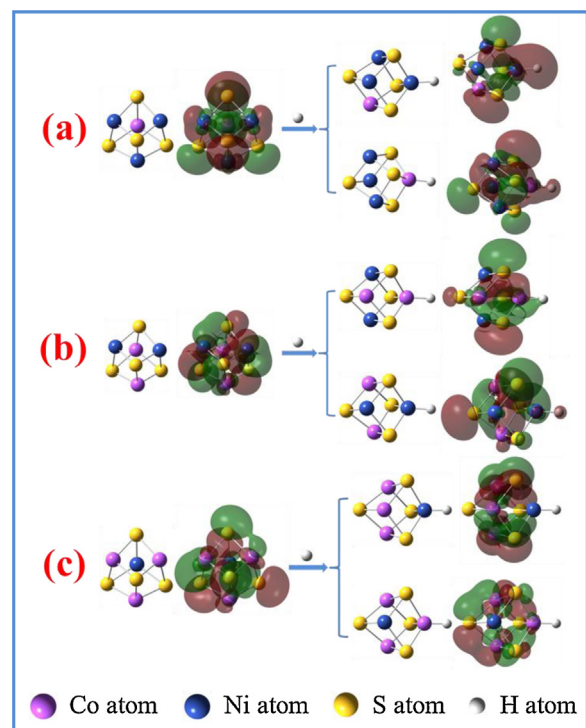


Fig. 1. The surface structure, H adsorption and charge density distribution of HOMO on CoNi_3S_4 (a), $\text{Co}_2\text{Ni}_2\text{S}_4$ (b), and Co_3NiS_4 (c), respectively.

$\text{Co}_x\text{Ni}_{4-x}\text{S}_4$ ($x = 1, 2, 3$) were shown in Fig. 1. Here, the configurations of all clusters were optimized by the B3LYP method of density functional theory (DFT) [40]. The structures and electronic energies calculation were completed by programs of Gaussian 09 and used LANL2DZ polar basis set for Co, Ni, 6-311G (d) basis set for S and H atoms. The calculation results of M ($\text{M} = \text{CoNi}_3\text{S}_4$, $\text{Co}_2\text{Ni}_2\text{S}_4$, Co_3NiS_4) and $\text{M}-\text{H}_{\text{ads}}$ were given in Table 1, where ΔG_{H} is the free energy of adsorbed hydrogen of $\text{M}-\text{H}_{\text{ads}}$. Generally, the molecular reaction can take place only if the energy difference between the HOMO and LUMO is less than 0.2205 a.u. (579 kJ mol^{-1}). The LUMO energy of free H_2O is about 66 kJ mol^{-1} , while the HOMO energy of $\text{Co}_x\text{Ni}_{4-x}\text{S}_4$, for example, $\text{Co}_2\text{Ni}_2\text{S}_4$, is about -368 kJ mol^{-1} , the energy gap (ΔE) between the HOMO of $\text{Co}_2\text{Ni}_2\text{S}_4$ and the LUMO of H_2O is 434 kJ mol^{-1} , which is less than 579 kJ mol^{-1} [41]. Comparing with results of CoNi_3S_4 and Co_3NiS_4 (488 and 518 kJ mol^{-1}), the ΔE of $\text{Co}_2\text{Ni}_2\text{S}_4$ was the lowest (434 kJ mol^{-1}). It indicated that the electrons transfer was possible from $\text{Co}_2\text{Ni}_2\text{S}_4$ nanocluster HOMO to LUMO of H_2O . The ΔG_{H} of $\text{Co}_2\text{Ni}_2\text{S}_4$ ($\text{Ni}-\text{H}_{\text{ads}}$) (506 kJ mol^{-1}) and $\text{Co}_2\text{Ni}_2\text{S}_4$ ($\text{Co}-\text{H}_{\text{ads}}$) (548 kJ mol^{-1}) were lower than the data of other $\text{Co}_x\text{Ni}_{4-x}\text{S}_4$ samples, which implied that $\text{Co}_2\text{Ni}_2\text{S}_4$ might show the higher activity than CoNi_3S_4 and Co_3NiS_4 . In those three structural units, the average distance ($\bar{d}_{\text{Co}-\text{Ni}}$) of Co and Ni in $\text{Co}_2\text{Ni}_2\text{S}_4$ was the shortest, which indicated that the optimized ratio of cobalt and nickel should be 1:1.

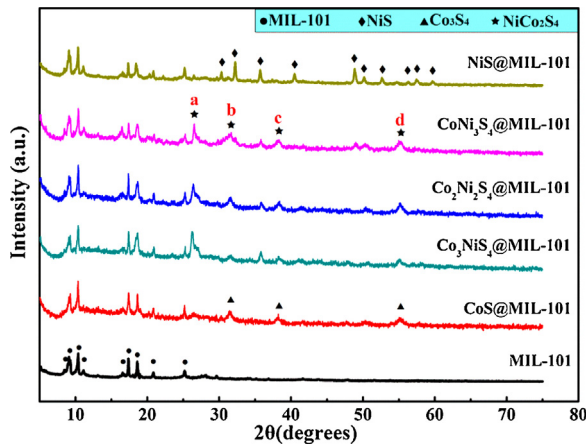
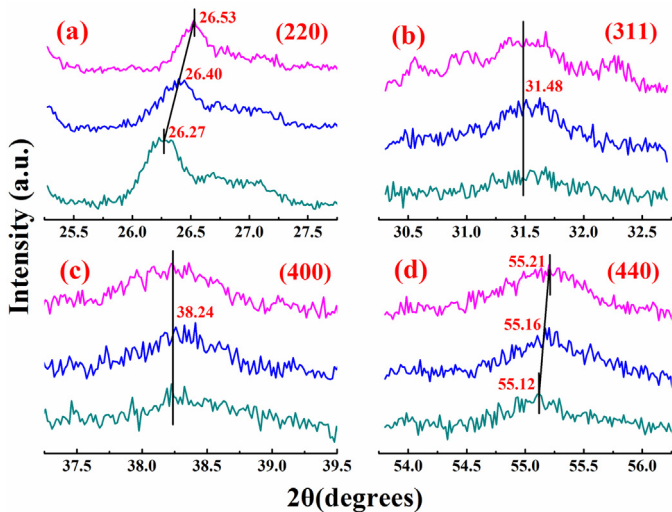
3.2. XRD analysis

Based on the analysis of DFT and FMOT calculations, a series of Co-Ni sulfide co-catalysts over MIL-101 (NiS@MIL-101 , $\text{CoNi}_3\text{S}_4@\text{MIL-101}$, $\text{Co}_2\text{Ni}_2\text{S}_4@\text{MIL-101}$, $\text{Co}_3\text{NiS}_4@\text{MIL-101}$ and CoS@MIL-101) were prepared via solvothermal method. The XRD patterns of catalysts were shown in Fig. 2. There are several typical peaks from 8 to 26° in the patterns of tested samples. The peaks at 8.5, 9.1, 10.4, 11.2, 16.6, 17.4, 18.6, 20.8, and 25.2° could be assigned to the diffraction peaks of MIL-101, which suggested that

Table 1

Calculated hydrogen adsorption energy of co-catalysts.

Catalysts	HOMO of catalysts (kJ mol ⁻¹)	ΔE (kJ mol ⁻¹)	ΔG _H (kJ mol ⁻¹)	-d _{Co-Ni} (Å)
CoNi ₃ S ₄	-422.3	488.3		2.9
Co ₂ Ni ₂ S ₄	-368.2	434.2		2.8
Co ₃ NiS ₄	-452.7	518.7		3.0
CoNi ₃ S ₄ (Co-H)	-576.5	642.5	827.0	
Co ₂ Ni ₂ S ₄ (Co-H)	-501.5	567.5	548.7	
Co ₃ NiS ₄ (Co-H)	-580.9	646.9	813.9	
CoNi ₃ S ₄ (Ni-H)	-570.8	636.8	960.9	
Co ₂ Ni ₂ S ₄ (Ni-H)	-471.4	537.4	506.7	
Co ₃ NiS ₄ (Ni-H)	-595.2	661.2	1073.8	

**Fig. 2.** XRD patterns of MIL-101, NiS@MIL-101, CoNi₃S₄@MIL-101, Co₂Ni₂S₄@MIL-101, Co₃NiS₄@MIL-101 and CoS@MIL-101.**Fig. 3.** Partial enlarged XRD patterns (a-d) of NiCo₂S₄ for CoNi₃S₄@MIL-101 (magenta curves), Co₂Ni₂S₄@MIL-101 (blue curves) and Co₃NiS₄@MIL-101 (dark cyan curves). (For interpretation of the references to colour in this figure legend, the reader is referred to the web version of this article.)

our MIL-101 framework was well crystalized. The peaks at 30.3, 32.2, 35.7, 40.5, 48.8, 50.1, 52.7, 56.3, 57.4 and 59.7° over NiS@MIL-101 belongs to the (101), (300), (021), (211), (131), (410), (321), (330) and (012) planes of NiS phase with a hexagonal structure (JCPDS# 86-2281), while the peaks at 31.5, 38.2, and 55.1° can be assigned to the (311), (400) and (440) planes of Co₃S₄ phase (JCPDS# 47-1738) over CoS@MIL-101, respectively. [42–45]

Fig. 3(a-d) showed partial enlarged XRD patterns of Fig. 2. The peaks at 31.48° and 38.24° in Fig. 3b and c could be assigned to (311)

and (400) planes of NiCo₂S₄ phase, while the main diffraction peaks appeared around 26° and 55° in Fig. 3a and d could be assigned to the cubic phase (220) and (440) of the NiCo₂S₄ phase over MIL-101 (JCPDS# 43-1477). [30,32,46,47] Very significant shift from 26.53° to 26.27° of (220) facet was observed over CoNi₃S₄@MIL-101, Co₂Ni₂S₄@MIL-101 and Co₃NiS₄@MIL-101 samples, at the same time, a weaker shift from 55.21° to 55.12° of (440) facet was also observed. These shifts were closely related to the Co content increase in Co_xNi_{4-x}S₄ nanocluster [21,39]. If the replacing Ni by Co takes place in the Co_xNi_{4-x}S₄ nanocluster, the interplanar spacing increase of (220) and (440) facet could occurred because the atomic radius of Co (1.67 Å) is larger than that of Ni (1.62 Å) (see Fig. S1) [48]. Besides, the strongest diffraction intensity of (220) facet indicated that (220) facet is the most probable exposed facet for the H⁺ adsorption and hydrogen generation over Co_xNi_{4-x}S₄ co-catalyst. (220) facet peak shift to small angles reflects such a change resulting from Co content increases. Because the (220), (440) and (110) are the equivalent crystal facet, it is reasonable to suppose that the state of chemisorbed H on (220) facet could be discussed on (110) facet over Co_xNi_{4-x}S₄ co-catalyst. As the results shown in Fig. S1, the bond lengths of d_{Co-H} and d_{Ni-H} are 1.70 Å and 1.75 Å respectively, which is less than 1.8 Å, indicating hydrogen formation is reasonable over adjacent sites on Co_xNi_{4-x}S₄ (110) surface (d_{H-H} < 1.8 Å). [9] Comparison the angles of chemisorbed H over cobalt or nickel over Co_xNi_{4-x}S₄ cluster, it is clear the data of Metal-H-H angle is the smallest in three Co_xNi_{4-x}S₄ samples, around 106.41° for Co-Co sites and 108.16° for Ni-Ni sites over Co₂Ni₂S₄. In this case, the distance between atom 5 and 6 (d₅₋₆) is 2.80 Å, which is well corresponding to the XRD pattern in Fig. 3a. Since the hydrogen formation is the controlling step in catalytic process, this small angle over Co₂Ni₂S₄ imply the corresponding surface intermediate is the most stable species. Such stable intermediates correspond to the 1:1 ratio of cobalt to nickel. In addition, the calculated electron density differences over Co_xNi_{4-x}S₄ surfaces in Fig. 1 also indicate a more stable species when the ratio of cobalt to nickel is 1:1 [49].

3.3. TEM analysis

The high-resolution transmission electron microscopy (HRTEM) images and the results of energy-dispersive X-ray (EDX) of the Co₂Ni₂S₄@MIL-101 samples are shown in Fig. 4. The morphology of MIL-101 was remained after Co₂Ni₂S₄ loading as shown in Fig. 4a-b [50]. HRTEM images indicated that the d-spacing between two adjacent lattice planes was about 0.481, 0.333, 0.284 and 0.167 nm (Fig. 4c-d). This value was in well agreement with the spacing of NiS (110), NiCo₂S₄ (220), NiCo₂S₄ (311) and NiCo₂S₄ (440) planes, respectively [51,52]. The angles between NiCo₂S₄ (220) and NiCo₂S₄ (311) planes were about 31.7 and 89.0°. The high-angle dark field scanning transmission electron microscopy (HAADF-STEM) images and EDX elemental mapping of Co₂Ni₂S₄@MIL-101 in Fig. 4e indicated that the distribution of C, O, Cr, S, Co and Ni elements were relatively homogeneous in Co₂Ni₂S₄@MIL-101. The

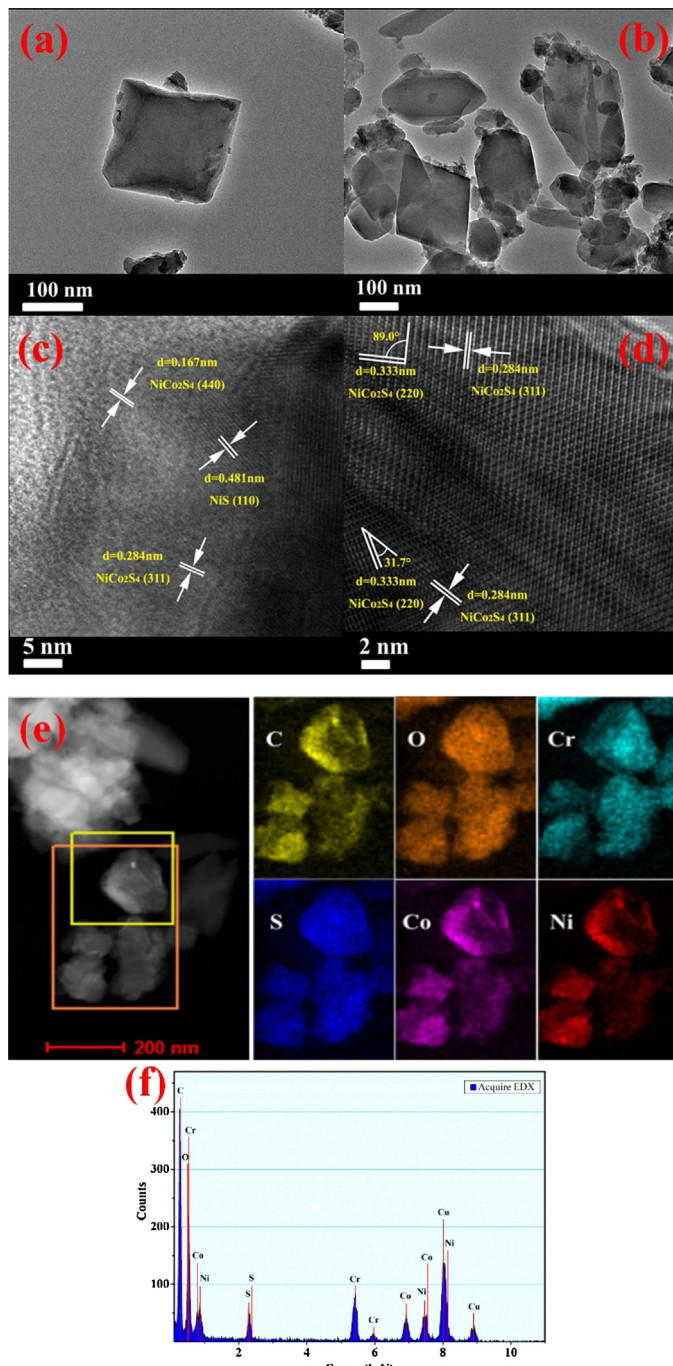


Fig. 4. TEM images of MIL-101 (a); TEM (b), HRTEM (c, d), HAADF-STEM and EDX elemental mapping (e) and EDX spectrum (f) for $\text{Co}_2\text{Ni}_2\text{S}_4@\text{MIL-101}$.

EDX measurement confirmed the co-existence of C, O, Cr, S, Co and Ni elements in $\text{Co}_2\text{Ni}_2\text{S}_4@\text{MIL-101}$ (Fig. 4f).

3.4. XPS and BET analysis

To further study the near-surface elemental composition and the chemical state in the as-prepared $\text{Co}_x\text{Ni}_{4-x}\text{S}_4@\text{MIL-101}$ composites, X-ray photoelectron spectroscopy (XPS) measurements were conducted and the results were presented in Fig. 5. The Co 2p XPS spectra of $\text{Co}_x\text{Ni}_{4-x}\text{S}_4@\text{MIL-101}$ (Fig. 5a) showed doublet line containing a low energy band (Co 2p_{3/2}) and a high energy band (Co 2p_{1/2}) at 778.5 and 793.5 eV [32]. Ni 2p XPS spectra (Fig. 5b) showed Ni 2p_{3/2} at 853.1 and Ni 2p_{1/2} at 870.4 eV. [53,54] S 2p XPS

Table 2
The atomic ratio of $\text{Co}_x\text{Ni}_{4-x}\text{S}_4@\text{MIL-101}$ measured by XPS.

Elements	C	O	Cr	Co	Ni	S
$\text{CoNi}_3\text{S}_4@\text{MIL-101}$	47.97	32.43	1.79	0.73	1.97	15.11
$\text{Co}_2\text{Ni}_2\text{S}_4@\text{MIL-101}$	47.31	32.53	1.83	1.31	1.44	15.58
$\text{Co}_3\text{Ni}_3\text{S}_4@\text{MIL-101}$	47.43	32.01	1.84	2.02	0.78	15.92

spectra showed the peaks at 161.1 eV and 162.3 eV, corresponding to the characteristic peaks of S^{2-} and the sulphur in low coordination state, respectively [30]. The peak at 168.5 eV might be ascribed to partially oxidized S or trace amount of sulfate on the surface (Fig. 5c). In $\text{CoNi}_3\text{S}_4@\text{MIL-101}$ and $\text{Co}_3\text{Ni}_3\text{S}_4@\text{MIL-101}$, the Co 2p_{3/2} shifted to 778.3 eV and 778.8 eV, while the Ni 2p_{3/2} shifted to 853.3 eV and 852.9 eV. These shifts reflect the subtle variation of surface state when Co contents change. Correspondingly, S 2p positively shifted 0.2 to 0.4 eV when Co contents change, respectively. According to calculation results in Table 1, the distance between Co and Ni over $\text{Co}_2\text{Ni}_2\text{S}_4$ was shorter ($\sim 2.8 \text{ \AA}$) than the data over other samples, which might lead to more effective charge separation in photo-induced hydrogen generation [55–57]. Consider the analysis in Fig. S1, the active sites over $\text{Co}_2\text{Ni}_2\text{S}_4@\text{MIL-101}$ may take advantages for stabilizing the intermediates during hydrogen formation.

Moreover, as the results of X-ray photoelectron spectroscopy characterization showed in Table 2, the Co and Ni atomic ratio of $\text{CoNi}_3\text{S}_4@\text{MIL-101}$ (0.73:1.97) is close to 1:3. Similarly, the Co and Ni atomic ratios of $\text{Co}_2\text{Ni}_2\text{S}_4@\text{MIL-101}$ and $\text{Co}_3\text{Ni}_3\text{S}_4@\text{MIL-101}$ are close to 1:1 and 3:1, respectively. That means NiS phase exists in $\text{CoNi}_3\text{S}_4@\text{MIL-101}$ and $\text{Co}_2\text{Ni}_2\text{S}_4@\text{MIL-101}$, while the CoS phase exists in $\text{Co}_3\text{Ni}_3\text{S}_4@\text{MIL-101}$. From XRD analysis of $\text{Co}_x\text{Ni}_{4-x}\text{S}_4@\text{MIL-101}$, this evidence is clearly consistent with quantification results obtained from XPS.

The Brunauer-Emmett-Teller specific surface areas (S_{BET}) were determined by N_2 isotherms at 77 K (as shown in Table 3). The S_{BET} of MIL-101, NiS@MIL-101, $\text{Co}_2\text{Ni}_2\text{S}_4@\text{MIL-101}$, and CoS@MIL-101 were 2713, 2398, 2483, and $2426 \text{ m}^2 \text{ g}^{-1}$, respectively. $\text{Co}_2\text{Ni}_2\text{S}_4@\text{MIL-101}$ has larger pore volume ($1.671 \text{ cm}^3 \text{ g}^{-1}$) and pore size (2.69 nm), which is benefit for NiCo_2S_4 particles loading in frameworks.

3.5. FTIR analysis and UV-vis absorption tests

Fig. S2 presented the FTIR spectra of MIL-101, NiS@MIL-101, $\text{CoNi}_3\text{S}_4@\text{MIL-101}$, $\text{Co}_2\text{Ni}_2\text{S}_4@\text{MIL-101}$, $\text{Co}_3\text{Ni}_3\text{S}_4@\text{MIL-101}$ and CoS@MIL-101. The strong absorption peak at 2353 cm^{-1} was due to the stretching vibrations of $\text{C}=\text{O}$ double bond. As for the spectrum of the parent MIL-101, sharp peaks with high intensity in the range of $1650\text{--}1350 \text{ cm}^{-1}$ could be assigned to the stretching vibrations of $\text{C}=\text{C}$ double bond of aromatic ring. The weak peak at 2970 cm^{-1} was $\text{C}-\text{H}$ stretching vibrations. Strong bands in the region of $1800\text{--}1300 \text{ cm}^{-1}$ corresponded to $\nu_{\text{as}}(\text{COO})$, $\nu_{\text{s}}(\text{COO})$, and $\nu(\text{C}-\text{C})$ vibrations implied the presence of dicarboxylate linker in the MIL-101 framework. Weak and narrow bands at 1016 and 745 cm^{-1} could be attributed to $\delta(\text{C}-\text{H})$ and $\gamma(\text{C}-\text{H})$ vibrations of aromatic rings, respectively, while the weak bands in the $700\text{--}400 \text{ cm}^{-1}$ were most likely due to the in-plane and out-of-plane bending modes of COO^- groups. The peak with medium strength at 582 cm^{-1} was $\text{Cr}-\text{O}$ vibrations, which proved that the metal organic framework was formed. The peak in $1650\text{--}1560 \text{ cm}^{-1}$ was related to the vibration of $\text{C}=\text{O}$ group. The broad peak in $3400\text{--}3000 \text{ cm}^{-1}$ range might due to crystalline water or the acidic OH of carbonyl group [58,59]. The results above indicated that the MIL-101 structure was remained after co-catalyst loading. Fig. S3 present the UV-vis diffuse reflectance absorption spectra of EY, EY sensitized MIL-101, NiS@MIL-101, $\text{Co}_2\text{Ni}_2\text{S}_4@\text{MIL-101}$, and CoS@MIL-101.

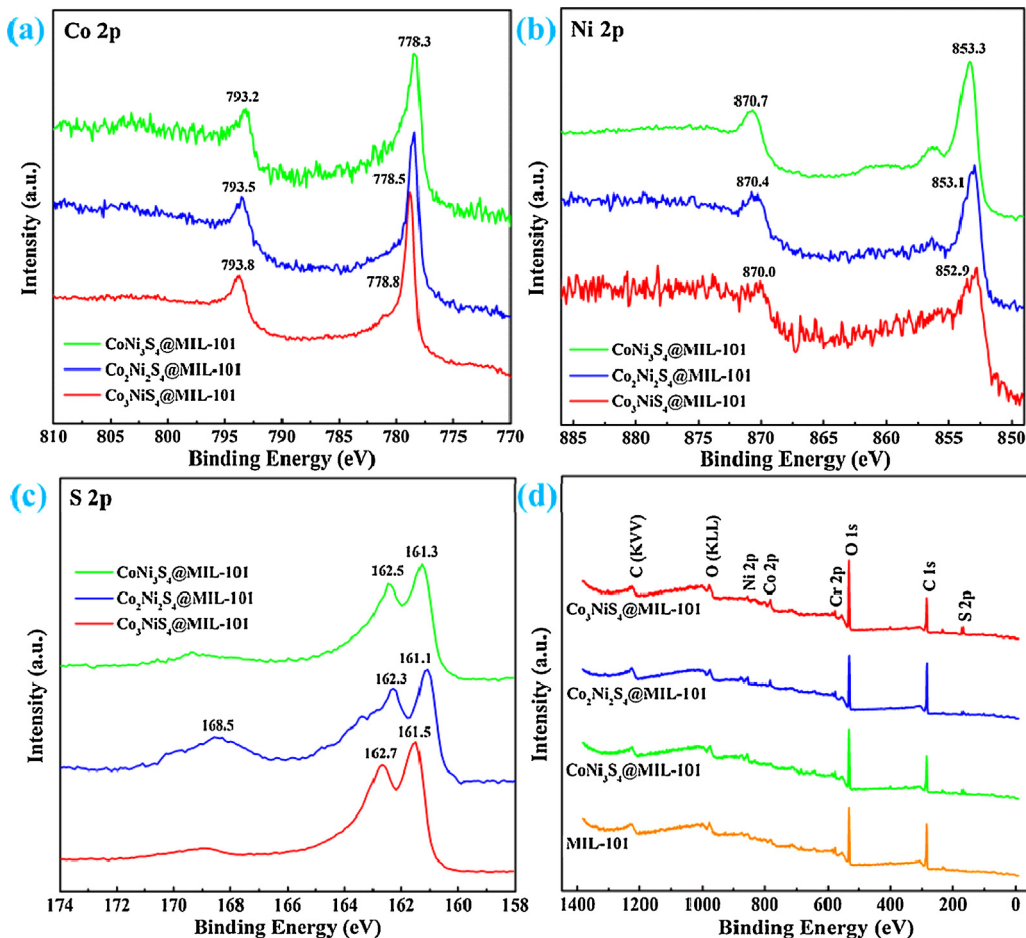


Fig. 5. Co 2p XPS spectra (a), Ni 2p XPS spectra (b) and S 2p XPS spectra (c) for $\text{CoNi}_3\text{S}_4@\text{MIL-101}$, $\text{Co}_2\text{Ni}_2\text{S}_4@\text{MIL-101}$ and $\text{Co}_3\text{NiS}_4@\text{MIL-101}$; XPS survey spectra (d) of $\text{CoNi}_3\text{S}_4@\text{MIL-101}$, $\text{Co}_2\text{Ni}_2\text{S}_4@\text{MIL-101}$, $\text{Co}_3\text{NiS}_4@\text{MIL-101}$ and MIL-101.

Table 3
Structural parameters obtained from N_2 adsorption isotherms analysis.

Samples	S_{BET} ($\text{m}^2 \text{ g}^{-1}$) ^a	Pore volume ($\text{cm}^3 \text{ g}^{-1}$) ^b	Average pore size (nm) ^b
MIL-101	2713	1.792	2.74
$\text{NiS}@\text{MIL-101}$	2398	1.544	2.57
$\text{Co}_2\text{Ni}_2\text{S}_4@\text{MIL-101}$	2483	1.671	2.69
$\text{CoS}@\text{MIL-101}$	2426	1.586	2.62

^a Obtained from BET method.

^b Total pore volume taken from the nitrogen adsorption volume at a relative pressure (P/P_0) of 0.99.

101 and $\text{CoS}@\text{MIL-101}$ samples. All the five samples exhibited obvious adsorption in the visible light range, which was due to the sensitization of the EY molecules. The maximum adsorption was at 518 nm, which was corresponding to the highest absorption of EY in the visible range.

To examine the optical properties of $\text{NiS}@\text{MIL-101}$, $\text{CoNi}_3\text{S}_4@\text{MIL-101}$, $\text{Co}_2\text{Ni}_2\text{S}_4@\text{MIL-101}$, $\text{Co}_3\text{NiS}_4@\text{MIL-101}$, $\text{CoS}@\text{MIL-101}$ and MIL-101, the spatial UV-vis diffused reflection absorption spectra were studied (Fig. S4a). It is clear that all of samples have a main effect on the optical property of light absorption near 350 nm. A series of catalysts have a main optical absorption shoulder near 350 nm. Catalyst samples exhibited rather flat absorption between 350 and 800 nm. This indicates that all of the catalysts are weakly responsive for visible light. It also proves that EY exhibits obviously enhanced light absorption capacity in the visible light region, which is necessary for efficient photocatalytic hydrogen generation. In addition, the band gaps (E_g) of $\text{CoNi}_3\text{S}_4@\text{MIL-101}$, $\text{Co}_2\text{Ni}_2\text{S}_4@\text{MIL-101}$, $\text{Co}_3\text{NiS}_4@\text{MIL-101}$

and MIL-101 were estimated to be 3.44, 3.31, 3.40 and 3.55 eV from the onset of the absorption curves (Fig. S4b), respectively, indicating that the absorption range of $\text{Co}_2\text{Ni}_2\text{S}_4@\text{MIL-101}$ was slightly enhanced. It also implies that the utilization of visible light for $\text{Co}_2\text{Ni}_2\text{S}_4@\text{MIL-101}$ is higher than other catalysts.

3.6. Photoluminescence intensity and fluorescence lifetime tests

To study the role of MIL-101 in photogenerated electrons transfer, the photoluminescence (PL) quenching in the presence of the MIL-101, $\text{NiS}@\text{MIL-101}$, $\text{CoNi}_3\text{S}_4@\text{MIL-101}$, $\text{Co}_2\text{Ni}_2\text{S}_4@\text{MIL-101}$, $\text{Co}_3\text{NiS}_4@\text{MIL-101}$ and $\text{CoS}@\text{MIL-101}$ were tested and the results were shown in Fig. 6. The aqueous EY-MIL-101 solution showed an intensive emission peak centered at 535 nm under 480 nm excitation, which was due to its strong recombination of excited charge pairs [60,61]. For the $\text{NiS}@\text{MIL-101}$, $\text{CoNi}_3\text{S}_4@\text{MIL-101}$, $\text{Co}_2\text{Ni}_2\text{S}_4@\text{MIL-101}$, $\text{Co}_3\text{NiS}_4@\text{MIL-101}$ and $\text{CoS}@\text{MIL-101}$ samples, there was a significant decrease in the peak intensity of EY emis-

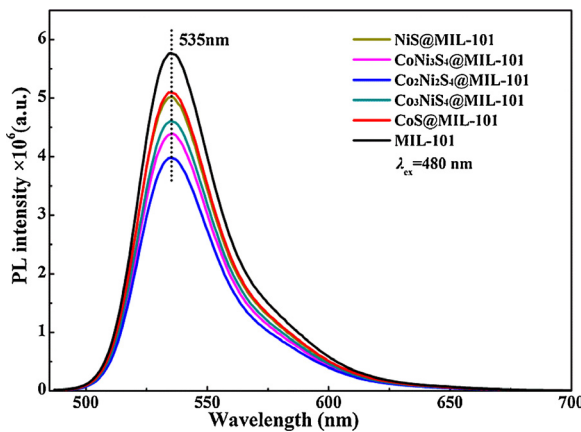


Fig. 6. Photoluminescence quenching (excitation wavelength of 480 nm) of EY (1.0×10^{-6} mol L $^{-1}$) by MIL-101, NiS@MIL-101, CoNiS₄@MIL-101, Co₂Ni₂S₄@MIL-101, Co₃NiS₄@MIL-101 and CoS@MIL-101 in 10% (v/v) TEOA aqueous solution at pH 9.

sion, and the corresponding peak intensity of Co₂Ni₂S₄@MIL-101 was the lowest, while the intensity of MIL-101 was the highest. These results suggested that excited charge recombination over Co₂Ni₂S₄@MIL-101 was slower than other catalysts, which might be attributed to the noncovalent π - π interaction of MIL-101 or NiCo₂S₄ with EY and the interfacial electron transfer from the attached EY* to the MIL-101 frameworks and NiCo₂S₄ surface. D. Tanaka et al. and Z. J. Zhang et al. previously reported MOFs with π -conjugated organic linkers could promote the charge transfer. They found that electron formed in dye molecule could transfer from the dye to the catalyst surface when dye adsorbed by offset face-to-face orientation *via* π - π conjugation between methylene blue (MB) and aromatic regions of the graphene [62,63]. Therefore it was reasonable that the electron transferred from excited dye to MIL-101 through the π - π interactions, and finally transferred to NiCo₂S₄ surface *via* similar mechanism.

The fluorescence lifetimes were obtained by fitting the decay profiles with one exponential term and two exponential terms, respectively. In Table 4, the emission of singlet excited EY gave a lifetime of 1.18 ns, which increased to 1.28 ns in the presence of NiS@MIL-101, 1.36 ns in CoNiS₄@MIL-101, 1.33 ns in Co₃NiS₄@MIL-101 and 1.24 ns in CoS@MIL-101. However, we observed an enhanced singlet excited state 1.49 ns in the Co₂Ni₂S₄@MIL-101 case. The fitted results with two exponential decay functions indicated the presence of dynamic quenching. The lifetimes of short and long decay components were 1.07 and 1.72 ns respectively. T. Lazarides et al. reported that the singlet fluorescence of dyes EY didn't quench when either TEOA or catalyst was added, which indicated that the singlet excited state did not take part in electron transfer [64]. The initially formed singlet excited state (EY^{1*}) changed to its lowest-lying triplet excited state (EY^{3*}) intermediates *via* intersystem crossing (ISC). These results indicated that MIL-101 could highly prolong the lifetime of the singlet excited EY^{1*} in the Co₂Ni₂S₄@MIL-101 systems, which could greatly promote the ISC to produce the low-lying triplet excited state (EY^{3*}) and then to form EY[•]. Due to the excellent electron transferring ability of MIL-101, electrons transferred from EY[•] to MIL-101 and active species (NiCo₂S₄) surface, where the protons were reduced to form molecular H₂.

3.7. Transient photocurrent-time and linear sweep voltammetry (LSV) tests

To provide additional evidence for the above suggested electron transfer mechanism, the transient photocurrent responses

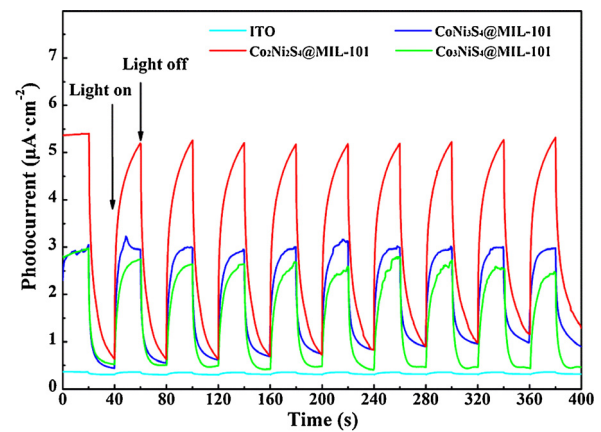


Fig. 7. Transient photocurrent-time profiles of EY-sensitized CoNiS₄@MIL-101, Co₂Ni₂S₄@MIL-101, Co₃NiS₄@MIL-101 coated on ITO glass in a mixed solution of 10% (v/v) TEOA and Na₂SO₄ (0.1 mol/L) at pH 9 under visible light irradiation ($\lambda \geq 420$ nm).

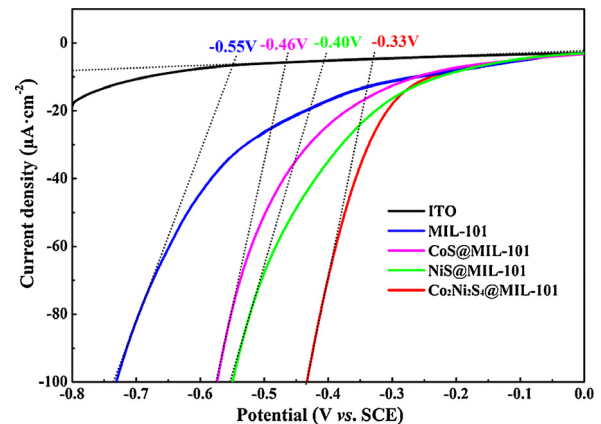


Fig. 8. LSV curves of bare ITO glass and MIL-101, NiS@MIL-101, Co₂Ni₂S₄@MIL-101 and CoS@MIL-101 coated on ITO electrodes in a mixed solution of 10% (v/v) TEOA and 0.1 mol/L Na₂SO₄ at pH 9. The scan rate was 1 mV s $^{-1}$.

of EY sensitized MIL-101, NiS@MIL-101, CoNiS₄@MIL-101, Co₂Ni₂S₄@MIL-101, Co₃NiS₄@MIL-101 and CoS@MIL-101 electrodes coated on ITO were recorded for several on-off cycles under visible light irradiation (Fig. S5). Obviously, the ITO/EY-NiS@MIL-101 and ITO/EY-CoS@MIL-101 electrodes showed significant photocurrent than photocurrent of ITO/EY-MIL-101, but the ITO/EY-Co₂Ni₂S₄@MIL-101 electrode exhibited the highest photocurrent (see Fig. 7). These results suggested the high H₂ production could be attributed to contribution of NiCo₂S₄ and fast interfacial electron transfer from EY[•] to Co₂Ni₂S₄@MIL-101. Optimized surface catalytic site over Co₂Ni₂S₄ co-catalyst might be the main reason for this excellent photo-current, just as discussed for the results in Fig. 3.

The electrochemical properties of ITO/EY-MIL-101, ITO/EY-NiS@MIL-101, ITO/EY-Co₂Ni₂S₄@MIL-101 and ITO/EY-CoS@MIL-101 electrodes were also investigated by the linear sweep voltammetry (LSV) technique (shown in Fig. 8). The cathodic current of ITO/EY-MIL-101 indicated that the MIL-101 material was a good carrier for the HER. Its overpotential was -0.55 V, however, NiS@MIL-101 and CoS@MIL-101, Co₂Ni₂S₄@MIL-101 electrodes exhibited -0.40 V, -0.46 V and -0.33 V respectively. Since the photocatalytic activity of hydrogen evolution was highly dependent on the overpotential of HER reaction [65], the low overpotential of Co₂Ni₂S₄@MIL-101 offered it better properties for photocatalytic hydrogen generation. Such a low overpotential of Co₂Ni₂S₄@MIL-

Table 4Decay Parameters of EY in the Presence of $\text{Co}_x\text{Ni}_{4-x}\text{S}_4@\text{MIL-101}$ ($x=0, 1, 2, 3, 4$) in 10% (v/v) TEOA aqueous Solution.

Systems	Lifetime, $\langle\tau\rangle$ (ns)	Pre-exponential factors A	Average lifetime, $\langle\tau\rangle$ (ns)	χ^2
EY	1.18	$A=0.074$	1.18	1.010
$\text{NiS}@\text{MIL-101}$	$\tau_1=0.61$ $\tau_2=1.48$	$A_1=0.041$ $A_2=0.055$	1.28	1.064
$\text{CoNi}_3\text{S}_4@\text{MIL-101}$	$\tau_1=0.95$ $\tau_2=1.65$	$A_1=0.065$ $A_2=0.054$	1.36	1.070
$\text{Co}_2\text{Ni}_2\text{S}_4@\text{MIL-101}$	$\tau_1=1.07$ $\tau_2=1.72$	$A_1=0.056$ $A_2=0.061$	1.49	1.066
$\text{Co}_3\text{NiS}_4@\text{MIL-101}$	$\tau_1=0.75$ $\tau_2=1.68$	$A_1=0.073$ $A_2=0.053$	1.33	1.079
$\text{CoS}@\text{MIL-101}$	$\tau_1=0.53$ $\tau_2=1.40$	$A_1=0.049$ $A_2=0.083$	1.24	1.112

^aDecay of TEOA aqueous solution (10% v/v) of 1.0×10^{-6} mol/L EY at pH 7 was recorded in the presence of 0.5 mg/L $\text{NiS}@\text{MIL-101}$, $\text{CoNi}_3\text{S}_4@\text{MIL-101}$ and $\text{CoS}@\text{MIL-101}$. The excited and emission wavelength were 480 nm, respectively.

^bSingle-exponential fit for EY.

^cDouble-exponential fit for $\text{EY-NiS}@\text{MIL-101}$, $\text{EY-CoNi}_3\text{S}_4@\text{MIL-101}$, $\text{EY-Co}_2\text{Ni}_2\text{S}_4@\text{MIL-101}$, $\text{EY-Co}_3\text{NiS}_4@\text{MIL-101}$ and $\text{EY-CoS}@\text{MIL-101}$.

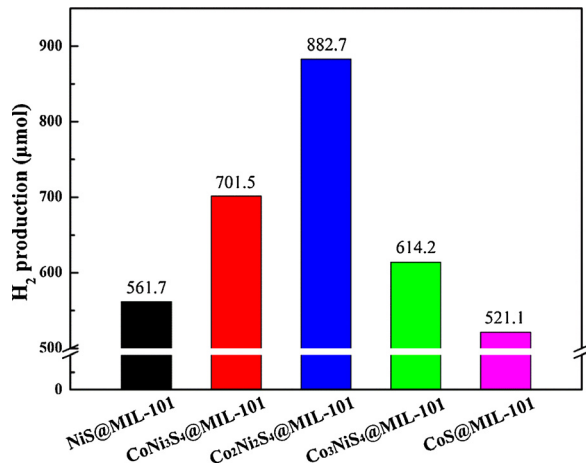


Fig. 9. The time courses of hydrogen evolution over $\text{NiS}@\text{MIL-101}$, $\text{CoNi}_3\text{S}_4@\text{MIL-101}$, $\text{Co}_2\text{Ni}_2\text{S}_4@\text{MIL-101}$, $\text{Co}_3\text{NiS}_4@\text{MIL-101}$ and $\text{CoS}@\text{MIL-101}$ photocatalysts in 100 mL 10% (v/v) TEOA aqueous solution (pH 9) under visible light irradiation ($\lambda \geq 420$ nm).

101 might due to the fast electrons transfer in MIL-101 and more stable intermediates during hydrogen formation over NiCo_2S_4 active surface.

3.8. HER photocatalytic performance and effect of pH on photocatalytic activity over $\text{Co}_2\text{Ni}_2\text{S}_4@\text{MIL-101}$

The photocatalytic activities for H_2 evolution were evaluated under visible light irradiation ($\lambda \geq 420$ nm) at pH 9. The time courses of H_2 evolution over different catalysts showed in Fig. 9. Only small amount of H_2 (561.7 and 521.1 μmol) was generated over the $\text{NiS}@\text{MIL-101}$ and $\text{CoS}@\text{MIL-101}$ co-catalysts after 120 min of irradiation. The amounts of H_2 generated over $\text{CoNi}_3\text{S}_4@\text{MIL-101}$ and $\text{Co}_3\text{NiS}_4@\text{MIL-101}$ were 701.5 and 614.2 μmol after 120 min of irradiation, respectively. $\text{Co}_2\text{Ni}_2\text{S}_4@\text{MIL-101}$ showed the highest photocatalytic performance, the amount of H_2 produced was 882.7 μmol in 120 min, which was 1.57 times higher than that of $\text{NiS}@\text{MIL-101}$ and 1.69 times higher than that of $\text{CoS}@\text{MIL-101}$ under the same reaction conditions. Fig. S6 presents the H_2 generation activity dependence on $\text{Co}_2\text{Ni}_2\text{S}_4$ loading amount, increase of $\text{Co}_2\text{Ni}_2\text{S}_4$ loading led to obvious increase of photocatalytic activity. Maximum photocatalytic activity reached 882.7 μmol in 120 min when the $\text{Co}_2\text{Ni}_2\text{S}_4$ loading was about 20%. Over-loading resulted in activity decrease, partially because of active species aggregation.

The photocatalytic activities for H_2 evolution were evaluated from EY (1.0×10^{-3} mol/L) photosensitized systems under visible

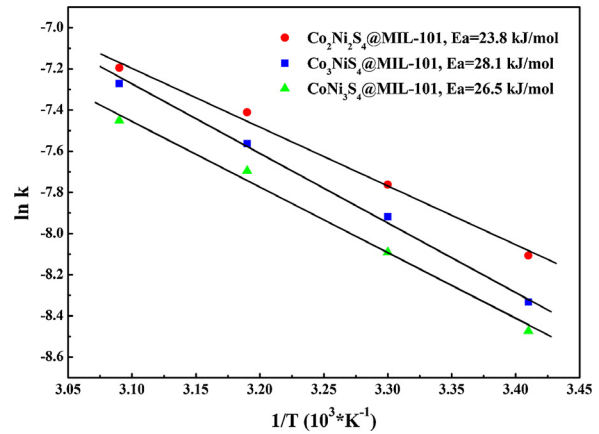


Fig. 10. Arrhenius plots obtained from EY (1.0×10^{-3} mol/L) photosensitized systems catalyzed by $\text{CoNi}_3\text{S}_4@\text{MIL-101}$, $\text{Co}_2\text{Ni}_2\text{S}_4@\text{MIL-101}$ and $\text{Co}_3\text{NiS}_4@\text{MIL-101}$ 100 mL of 10% (v/v) TEOA aqueous solution under visible light irradiation ($\lambda \geq 420$ nm) under different temperatures.

light irradiation ($\lambda \geq 420$ nm) at pH 9. The time courses of H_2 evolution over different catalysts without loading MIL-101 showed in Fig. S7. $\text{Co}_2\text{Ni}_2\text{S}_4$ showed the highest photocatalytic performance, the amount of H_2 produced was 818.9 μmol in 120 min. It is probably due to forming like *p-n* heterojunctions structure by modulation of Co-Ni ratio, which enhances photocatalytic performance on hydrogen generation. The decreasing amounts of H_2 produced over the remaining catalysts were 702.1, 663.4, 634.0, 487.3 and 339.0 μmol in 120 min, representing NiCo_2S_4 , CoNi_3S_4 , Co_3NiS_4 , NiS and CoS samples, respectively. No hydrogen over MIL-101 in 120 min under irradiation of visible light was detected. It proves that $\text{Co}_2\text{Ni}_2\text{S}_4$ is an excellent cocatalyst, which suggests $\text{Co}_2\text{Ni}_2\text{S}_4@\text{MIL-101}$ also have high efficiency for visible photocatalytic hydrogen generation. Furthermore, photocatalytic activities for H_2 evolution were evaluated from EY (1.0×10^{-3} mol/L) photosensitized systems catalyzed by series of catalysts under visible light irradiation ($\lambda \geq 420$ nm) at pH 9. As the results shown in Fig. S8, the amount of H_2 produced over cocatalyst@MIL-101 is about 5–6 times than pure cocatalyst without MIL-101 carries. It indicates that MIL-101 plays an important role on terms of electron transfer, which ensures electron fast transfer to cocatalyst surface. Comparing EY-sensitized system, the unsensitized system shows a very low photocatalytic performance. The amounts of H_2 generated over $\text{CoNi}_3\text{S}_4@\text{MIL-101}$, $\text{Co}_2\text{Ni}_2\text{S}_4@\text{MIL-101}$ and $\text{Co}_3\text{NiS}_4@\text{MIL-101}$ are 0.177, 0.262 and 0.156 μmol after 120 min of irradiation, respectively (Fig. S9).

Fig. 10 gave the activation energies of $\text{Co}_x\text{Ni}_{4-x}\text{S}_4@\text{MIL-101}$ calculated from the slope of the linear $\ln k$ vs $1000/T$

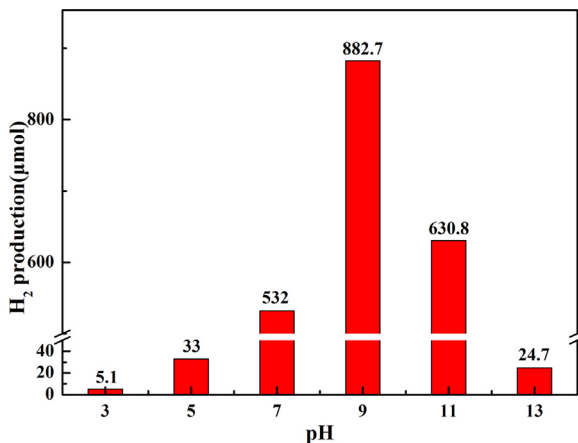


Fig. 11. Effect of pH value on photocatalytic rate of H₂ evolution over EY-Co₂Ni₂S₄@MIL-101 photocatalyst in 100 mL 10% (v/v) TEOA aqueous solution under visible light irradiation ($\lambda \geq 420$ nm). EY: 1.0×10^{-3} mol/L.

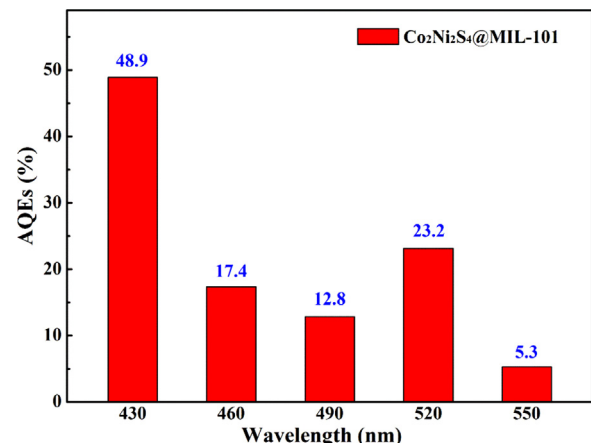


Fig. 12. Apparent quantum efficiencies (AQEs) of H₂ evolution for EY (1.0 $\times 10^{-3}$ mol/L) photosensitized systems catalyzed by Co₂Ni₂S₄@MIL-101 in 100 mL 10% (v/v) TEOA aqueous solution (pH 9) under light irradiation with different wavelengths. The system was irradiated by a 300-W Xe lamp with a band pass filter of 420 nm and a band pass filter. Irradiation time: 30 min.

dependence ($E_a = -\text{slope}/R$). The apparent activation energies of Co_xNi_{4-x}S₄@MIL-101 series samples followed this order: Co₂Ni₂S₄@MIL-101 (23.8 kJ/mol) < CoNi₃S₄@MIL-101 (26.5 kJ/mol) < Co₃Ni₂S₄@MIL-101 (28.1 kJ/mol). It is obvious that the modulation of Co-Ni ratio has significantly influence on the apparent activation energy of photocatalytic HER. Comparatively, the lower activation energy catalyst indicates that the HER is easier to take place, which also implies efficient catalytic activity for hydrogen generation when Co/Ni ratio is 1:1.

It was known that the solution pH had significant influence on photocatalytic activity. As shown in Fig. 11, the rate of hydrogen evolution maximized (441.4 $\mu\text{mol h}^{-1}$) at pH 9 and decreased dramatically both under more acidic and basic reaction conditions. The decrease of rate of hydrogen evolution at acidic pH likely resulted from the protonation of TEOA, which was a less effective electron donor, thus leading to a shorter lifetime of the excited EY and lower efficiency of the excited dye species. Under strong basic condition, the thermodynamic driving force for hydrogen evolution from water decreased due to the lower concentration of H⁺.

3.9. Apparent quantum efficiencies and stability

To investigate the wavelength dependence of photocatalytic H₂ evolution, the apparent quantum efficiencies (AQEs) of Co₂Ni₂S₄@MIL-101 for hydrogen generation were examined over a wide visible light range of 430–550 nm. As shown in Fig. 12, the highest AQEs of EY-Co₂Ni₂S₄@MIL-101 was 48.9% (at 430 nm). Meanwhile, the AQEs under other wavelengths irradiation were 17.4% (460 nm), 12.8% (490 nm), 23.2% (520 nm) and 5.3% (550 nm), respectively. The AQEs at 430 nm might ascribe to its stronger photon energy, while the high AQEs at 520 nm might result from the stronger absorbance of EY [60].

The stability tests of Co₂Ni₂S₄@MIL-101 were measured, and the result was shown in Fig. 13. In the first cycle, the maximum amounts of photocatalytic H₂ evolution over Co₂Ni₂S₄@MIL-101 was 864.8 μmol . The co-catalyst was collected from the reaction mixture by filtration, after adding fresh EY and TEOA. The H₂ evolution activity of Co₂Ni₂S₄@MIL-101 could be revived to 97% in the second run. The activity gradually reduced in the next two runs, due to the loss of catalyst during washing and filtration. Hence, Co₂Ni₂S₄@MIL-101 was still relatively stable during the photocatalytic H₂ evolution.

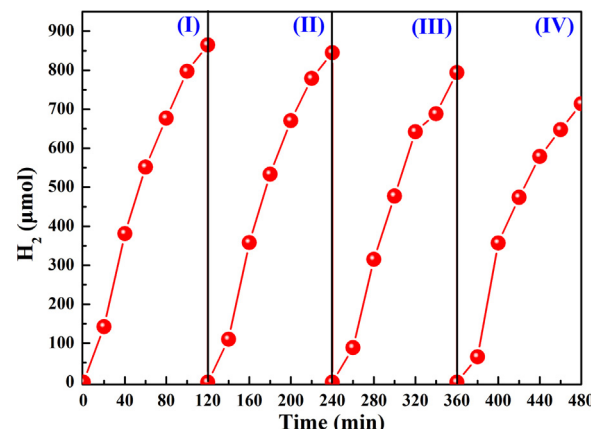
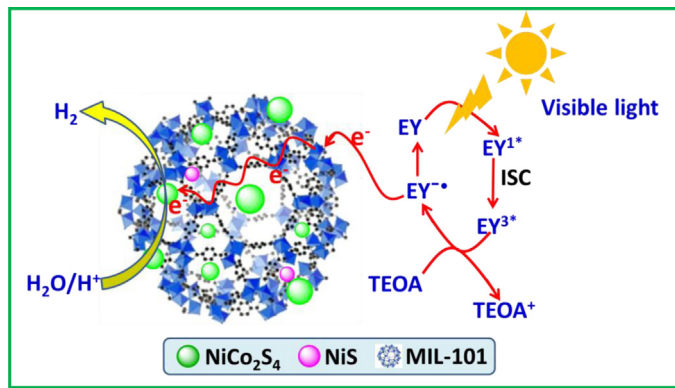


Fig. 13. Stability test and comparison of H₂ evolution over EY sensitized Co₂Ni₂S₄@MIL-101 (red ball) in 100 mL 10% (v/v) TEOA aqueous solution (pH 9) under visible light irradiation ($\lambda \geq 420$ nm). The reaction was continued for 480 min, with evacuation every 120 min. (I) First run; (II) add EY and TEOA, and evacuation; (III) repeat II; (IV) repeat III. The system was irradiated by a 300-W Xe lamp with an optical cut-off filter of 420 nm. (For interpretation of the references to colour in this figure legend, the reader is referred to the web version of this article.)

3.10. Photocatalytic mechanism for H₂ evolution over Co₂Ni₂S₄@MIL-101

The high H₂ evolution activity of the Co₂Ni₂S₄@MIL-101 catalyst in a dye-sensitized system can be depicted in Scheme 1. MIL-101 has surprisingly large surface area of $\sim 2713 \text{ m}^2 \text{ g}^{-1}$, specific structures, and is conducive to the electron transfer. Under visible light irradiation, the EY absorbs light photon to form singlet excited state EY^{1*}, which subsequently produces a lowest-lying triplet excited state EY^{3*} via an efficient ISC. In the presence of TEOA as a sacrificial donor, EY^{3*} can be reductively quenched and produce EY^{•-} [64,66,67]. These EY^{•-} species preferentially transfer their electrons to the MIL-101 frameworks due to its electron transport characteristics. The accumulated electrons on the MIL-101 frameworks will transfer to the active species (NiCo₂S₄), and finally H⁺ obtains electrons from NiCo₂S₄ to form hydrogen. MIL-101 can function as an excellent electron acceptor and transporter to efficiently prolong the lifetime of charge carriers and conse-



Scheme 1. Photocatalytic mechanism for H_2 evolution over the EY sensitized $Co_2Ni_2S_4@MIL-101$ under visible light irradiation.

quently improve the charge separation efficiency and the catalytic H_2 evolution activity of the $Co_2Ni_2S_4@MIL-101$.

4. Conclusions

In summary, we designed low adsorption energy sulfide composites using DFT and FMOT theory calculation analysis and prepared high activity and low overpotential co-catalyst $Co_xNi_{4-x}S_4$ nanoparticles anchored on the frameworks of MIL-101, which provide more catalytically favorable surface atomic structures and fast electron transfer route. Lower hydrogen absorption also enhanced photocatalytic hydrogen generation. Compared with simple sulphide co-catalyst, the dual transition metal sulfide $Co_2Ni_2S_4@MIL-101$ as co-catalyst exhibited the highest photocatalytic activity after sensitized by EY (the amount of H_2 was $882.7 \mu\text{mol}$ in 120 min) and AQEs ($\sim 48.9\%$) under 430 nm illuminations at pH 9. The results of the electrochemical and fluorescence measurements indicated that the $Co_2Ni_2S_4@MIL-101$ exhibited a larger transient photocurrent, lower overpotential (-0.33 V) and longer fluorescence lifetime (1.49 ns). Dual transition metal sulfide $Co_2Ni_2S_4@MIL-101$ with low hydrogen adsorption energy exhibited superior photocatalytic performance, offered suitable active site for hydrogen adsorption and led to stable reaction intermediate formation, which was expected to replace the precious metals.

Acknowledgements

The authors are thankful for the support of the NSFC (Grant Nos. 21433007 and 21673262) and 973 Program of China (No. 2013CB632404).

Appendix A. Supplementary data

Supplementary data associated with this article can be found, in the online version, at <http://dx.doi.org/10.1016/j.apcatb.2017.01.048>.

References

- [1] K.I. Zamaraev, V.N. Parmon, *Catal. Rev.* 22 (1980) 261–324.
- [2] J.A. Turner, *Science* 305 (2004) 972–974.
- [3] L. Zhang, H.B. Wu, Y. Yan, X. Wang, X.W. Lou, *Energy Environ. Sci.* 7 (2014) 3302–3306.
- [4] M. Cagnello, A. Gasparotto, V. Gombac, T. Montini, *Eur. J. Inorg. Chem.* 28 (2011) 4309–4323.
- [5] R.H. Crabtree, M.F. Mellea, J.M. Mihelcic, J.M. Quirk, *J. Am. Chem. Soc.* 104 (1982) 107–113.
- [6] S. Zinoviev, F. Müller-Langer, P. Das, N. Bertero, P. Fornasiero, M. Kaltschmitt, G. Centi, S. Miertus, *ChemSusChem* 3 (2010) 1106–1133.
- [7] X. Chen, S. Shen, L. Guo, S.S. Mao, *Chem. Rev.* 110 (2010) 6503–6570.
- [8] Y. Wang, Y. Wang, R. Xu, *J. Phys. Chem. C* 117 (2013) 783–790.
- [9] Z. Li, C. Kong, G. Lu, *Int. J. Hydrogen Energy* 40 (2015) 9061–9068.
- [10] M. Elvington, J. Brown, S.M. Arachchige, K.J. Brewer, *J. Am. Chem. Soc.* 129 (2007) 10644–10645.
- [11] G. Zhou, R. Dou, H. Bi, S. Xie, Y. Pei, K. Fan, M. Qiao, B. Sun, B. Zong, *J. Catal.* 332 (2015) 119–126.
- [12] B. Tian, Z. Li, W. Chen, G. Lu, *J. Phys. Chem. C* 120 (2016) 6409–6415.
- [13] P. He, Y. Chen, W. Fu, *J. Mol. Catal. (China)* 30 (2016) 269–275.
- [14] C. Li, Z. Lei, Q. Wang, F. Cao, F. Wang, W. Shanguan, *J. Mol. Catal. (China)* 29 (2015) 381–389.
- [15] Y. Li, H. Wang, L. Xie, Y. Liang, G. Hong, H. Dai, *J. Am. Chem. Soc.* 133 (2011) 7296–7299.
- [16] C. Kong, S. Min, G. Lu, *ACS Catal.* 4 (2014) 2763–2769.
- [17] W.-T. Sun, Y. Yu, H.-Y. Pan, X.-F. Gao, Q. Chen, L.-M. Peng, *J. Am. Chem. Soc.* 130 (2008) 1124–1125.
- [18] X. Long, G. Li, Z. Wang, H. Zhu, T. Zhang, S. Xiao, W. Guo, S. Yang, *J. Am. Chem. Soc.* 137 (2015) 11900–11903.
- [19] G.K. Mor, O.K. Varghese, R.H.T. Wilke, S. Sharma, K. Shankar, T.J. Latempa, K.-S. Choi, C.A. Grimes, *Nano Lett.* 8 (2008) 1906–1911.
- [20] Y. Chen, S. Zhao, X. Wang, Q. Peng, R. Lin, Y. Wang, R. Shen, X. Cao, L. Zhang, G. Zhou, J. Li, A. Xia, Y. Li, *J. Am. Chem. Soc.* 138 (2016) 4286–4289.
- [21] M. Liu, D. Jing, Z. Zhou, L. Guo, *Nat. Commun.* 4 (2013) 2278.
- [22] A. Kudo, Y. Miseki, *Chem. Soc. Rev.* 38 (2009) 253–278.
- [23] S.V. Patwardhan, F.S. Emami, R.J. Berry, S.E. Jones, R.R. Naik, O. Deschaume, H. Heinz, C.C. Perry, *J. Am. Chem. Soc.* 134 (2012) 6244–6256.
- [24] W. Zhen, H. Gao, B. Tian, J. Ma, G. Lu, *ACS Appl. Mater. Interfaces* 8 (2016) 10808–10819.
- [25] C. Kong, S. Min, G. Lu, *Chem. Commun.* 50 (2014) 5037–5039.
- [26] Y. Zheng, Y. Jiao, Y. Zhu, L.H. Li, Y. Han, Y. Chen, A. Du, M. Jaroniec, S.Z. Qiao, *Nat. Commun.* 5 (2014) 3783.
- [27] N.M. Marković, B.N. Grgur, P.N. Ross, *J. Phys. Chem. B* 101 (1997) 5405–5413.
- [28] W. Zhou, H. Wu, T. Yildirim, *J. Am. Chem. Soc.* 130 (2008) 15268–15269.
- [29] J.K. Nørskov, M. Scheffler, H. Toulih, *MRM Bull.* 31 (2006) 669–674.
- [30] H. Chen, J. Jiang, L. Zhang, H. Wan, T. Qi, D. Xia, *Nanoscale* 5 (2013) 8879–8883.
- [31] J. Xiao, X. Zeng, W. Chen, F. Xiao, S. Wang, *Chem. Commun.* 49 (2013) 11734–11736.
- [32] J. Xiao, L. Wan, S. Yang, F. Xiao, S. Wang, *Nano Lett.* 14 (2014) 831–838.
- [33] K. Meyer, M. Ranocchiari, J.A. van Bokhoven, *Energy Environ. Sci.* 8 (2015) 1923–1937.
- [34] W. Zhen, J. Ma, G. Lu, *Appl. Catal. B* 190 (2016) 12–25.
- [35] W. Wang, G. Wang, *J. Mol. Catal. (China)* 29 (2015) 275–287.
- [36] G. Férey, C. Mellot-Draznieks, C. Serre, F. Millange, J. Dutour, S. Surblé, I. Margioliaki, *Science* 309 (2005) 2040–2042.
- [37] Q.-L. Zhu, J. Li, Q. Xu, *J. Am. Chem. Soc.* 135 (2013) 10210–10213.
- [38] N. Cao, L. Yang, H. Dai, T. Liu, J. Su, X. Wu, W. Luo, G. Cheng, *Inorg. Chem.* 53 (2014) 10122–10128.
- [39] J. Wang, P. Yang, J. Zhao, Z. Zhu, *Appl. Surf. Sci.* 282 (2013) 930–936.
- [40] P.B. Balbuena, D. Altomare, L. Agapito, J.M. Seminario, *J. Phys. Chem. B* 107 (2003) 13671–13680.
- [41] Z.D. Wei, A.Z. Yan, Y.C. Feng, L. Li, C.X. Sun, Z.G. Shao, P.K. Shen, *Electrochim. Commun.* 9 (2007) 2709–2715.
- [42] Y. Liao, K. Pan, Q. Pan, G. Wang, W. Zhou, H. Fu, *Nanoscale* 7 (2015) 1623–1626.
- [43] C. Sun, M. Ma, J. Yang, Y. Zhang, P. Chen, W. Huang, X. Dong, *Sci. Rep.* 4 (2014) 7054.
- [44] Y. Du, X. Zhu, X. Zhou, L. Hu, Z. Dai, J. Bao, *J. Mater. Chem. A* 3 (2015) 6787–6791.
- [45] Q. Wang, L. Jiao, H. Du, Y. Si, Y. Wang, H. Yuan, *J. Mater. Chem.* 22 (2012) 21387–21391.
- [46] Y. Liu, J. Zhang, S. Wang, K. Wang, Z. Chen, Q. Xu, *New J. Chem.* 38 (2014) 4045–4048.
- [47] L. Niu, Y. Wang, F. Ruan, C. Shen, S. Shan, M. Xu, Z. Sun, C. Li, X. Liu, Y. Gong, *J. Mater. Chem. A* 4 (2016) 5669–5677.
- [48] X. Wang, J. Stöver, V. Zilas, L. Altmann, K. Thiel, K. Al-Shamery, M. Bäumer, H. Borchert, J. Parisi, J. Kolny-Olesiak, *Langmuir* 27 (2011) 11052–11061.
- [49] M.J.F. Martins, A.R. Ferreira, E. Konstantinova, H.A. de Abreu, W.F. Souza, S.S.X. Chiaro, L.G. Dias, A.A. Leitão, *Int. J. Quantum Chem.* 112 (2012) 3234–3239.
- [50] S.H. Jhung, J.H. Lee, J.W. Yoon, C. Serre, G. Férey, J.S. Chang, *Adv. Mater.* 19 (2007) 121–124.
- [51] Q. Liu, J. Jin, J. Zhang, *ACS Appl. Mater. Interfaces* 5 (2013) 5002–5008.
- [52] M. Sun, J. Tie, G. Cheng, T. Lin, S. Peng, F. Deng, F. Ye, L. Yu, *J. Mater. Chem. A* 3 (2015) 1730–1736.
- [53] A.-Q. Wang, J.-H. Liu, S.D. Lin, T.-S. Lin, C.-Y. Mou, *J. Catal.* 233 (2005) 186–197.
- [54] P.A.P. Nascente, S.G.C. de Castro, R. Landers, G.G. Kleiman, *Phys. Rev. B* 43 (1991) 4659–4666.
- [55] M. Ding, B.H.W.S. de Jong, S.J. Roosendaal, A. Vredenberg, *Geochim. Cosmochim. Acta* 64 (2000) 1209–1219.
- [56] A.P. Grosvenor, B.A. Kobe, M.C. Biesinger, N.S. McIntyre, *Surf. Interface Anal.* 36 (2004) 1564–1574.
- [57] M.C. Biesinger, L.W.M. Lau, A.R. Gerson, R.S.C. Smart, *Phys. Chem. Chem. Phys.* 14 (2012) 2434–2442.
- [58] T.M. Reineke, M. Eddaoudi, M. Fehr, D. Kelley, O.M. Yaghi, *J. Am. Chem. Soc.* 121 (1999) 1651–1657.
- [59] L. Huang, H. Wang, J. Chen, Z. Wang, J. Sun, D. Zhao, Y. Yan, *Microporous Mesoporous Mater.* 58 (2003) 105–114.
- [60] S. Min, G. Lu, *J. Phys. Chem. C* 115 (2011) 13938–13945.

- [61] Q. Li, L. Chen, G. Lu, *J. Phys. Chem. C* 111 (2007) 11494–11499.
- [62] D. Tanaka, S. Horike, S. Kitagawa, M. Ohba, M. Hasegawa, Y. Ozawa, K. Toriumi, *Chem. Commun.* (2007) 3142–3144.
- [63] Z. Zhang, S. Xiang, X. Rao, Q. Zheng, F.R. Fronczek, G. Qian, B. Chen, *Chem. Commun.* 46 (2010) 7205–7207.
- [64] T. Lazarides, T. McCormick, P. Du, G. Luo, B. Lindley, R. Eisenberg, *J. Am. Chem. Soc.* 131 (2009) 9192–9194.
- [65] H. Ezaki, M. Morinaga, S. Watanabe, *Electrochim. Acta* 38 (1993) 557–564.
- [66] W. Zhang, J. Hong, J. Zheng, Z. Huang, J. Zhou, R. Xu, *J. Am. Chem. Soc.* 133 (2011) 20680–20683.
- [67] D.-Y. Wang, M. Gong, H.-L. Chou, C.-J. Pan, H.-A. Chen, Y. Wu, M.-C. Lin, M. Guan, J. Yang, C.-W. Chen, Y.-L. Wang, B.-J. Hwang, C.-C. Chen, H. Dai, *J. Am. Chem. Soc.* 137 (2015) 1587–1592.